Check for updates

JGR Oceans

RESEARCH ARTICLE
10.1029/2021JC017984

A Mesoscale Eddy With Submesoscale Spiral Bands Observed From Seismic Reflection Sections in the Northwind Basin, Arctic Ocean

Shun Yang[1], Haibin Song[1], Bernard Coakley[2], Kun Zhang[1], and Wenhao Fan[1]

[1]School of Ocean and Earth Science, Tongji University, Shanghai, China, [2]Geophysical Institute, University of Alaska, Fairbanks, AK, USA

Key Points:

- A mesoscale anticyclonic eddy was observed from simultaneous seismic and current velocity data in the Northwind Basin, Arctic Ocean
- This eddy had a core with a diameter of ~26 km, a height of 250 m, and was surrounded by submesoscale spiral bands with large slopes
- This eddy had a rigid core with a rotation period of about 26 hr and a westward advection velocity of about 1 cm s^{-1}

Correspondence to:
H. Song,
hbsong@tongji.edu.cn

Citation:
Yang, S., Song, H., Coakley, B., Zhang, K., & Fan, W. (2022). A mesoscale eddy with submesoscale spiral bands observed from seismic reflection sections in the Northwind Basin, Arctic Ocean. *Journal of Geophysical Research: Oceans*, *127*, e2021JC017984. https://doi.org/10.1029/2021JC017984

Received 8 SEP 2021
Accepted 7 MAR 2022

© 2022. American Geophysical Union. All Rights Reserved.

Abstract The Arctic Ocean is well-known for its large number of mesoscale eddies. We observed a lens-shaped mesoscale eddy by using two roughly perpendicular multichannel reflection seismic sections collected in the Northwind Basin, Arctic Ocean in late September 2011. This is the first seismic imaging of the water column in the Arctic Ocean. The two lines were acquired about seven days apart. The eddy had a horizontal scale of ~56 km and extended from near-surface to 300 m. The thickness of the eddy was ~250 m. The eddy core, characterized by weak reflections, has a radius of ~13 km. The volume of core water was ~89 km^3. The horizontal current velocity collected by acoustic Doppler current profiler simultaneously with the seismic data shows that the eddy had a rigid core with a rotation period of ~26 hr, and max azimuthal velocities of 0.59 m s^{-1}. The velocity outside the core decreased in a quadratic inverse curve with the radius. During the observation, the eddy moved westward with an advection velocity of ~1 cm s^{-1}, and the net transport of the core water was about 0.05 Sv. There were multi-arm structures at the boundaries of the eddy, forming submesoscale spiral bands. The steep spiral arms (dip angle can be up to ~4°) may be caused by eddy stirring. Seismic observations provide important insights into our understanding of the vertical structure of ocean eddies, the horizontal and vertical transport of matter, and fluxes of heat that can cause sea ice melting in the Arctic Ocean.

Plain Language Summary Large eddies in the ocean share some features with tropical cyclones, including the presence of spiral arms extending outwards from a clear core. For tropical cyclones, these arms are easily seen in satellite images as rain bands. In the ocean, spiral eddies can sometimes be seen in satellite maps of ocean surface temperature and sea ice distribution. However, to understand the role of these features in the ocean, we need observations that extend well below the surface. We use the seismic reflection method, similar to how it is employed by the petroleum industry, to observe the high-resolution vertical structures of the spiral bands of an eddy in the Arctic Ocean. We employ specialized processing methods to reveal this eddy and estimate its role in transport of material. These data will improve our understanding of the vertical structure of ocean eddies and the horizontal and vertical transports of matter, and the transport of ocean heat that affects sea ice melting in the Arctic Ocean.

1. Introduction

Oceanic eddies play an important role in the long-distance transport and redistribution of ocean materials and energy (Z. G. Zhang et al., 2014). There are a large number of mesoscale eddies in the Arctic Ocean (D'Asaro, 1988b; Manley & Hunkins, 1985; Spall et al., 2008; Zhao et al., 2014). In the Beaufort Sea, mesoscale eddies can occupy at least 25% of the sea surface area (Manley & Hunkins, 1985). Many eddies are limited to the upper 250 m, with the maximum depth being restricted by the halocline (Zhao et al., 2014). Due to the severe weather conditions and perennial sea ice cover, however, it is difficult to observe Arctic Ocean eddies, limiting our understanding of their role in lateral and vertical transport of matter, heat, and energy in the Arctic.

The formation mechanisms of these shallow eddies include the increase of the density of local water in polynyas (Muench et al., 2000), instabilities of the fronts (X. Zhang et al., 2019), instabilities of the shelf break jet (Spall et al., 2008), and interaction between flow and topography (D'Asaro, 1988a). With the development of remote sensing technology, a large number of eddies in the Arctic Ocean have been observed from Synthetic Aperture Radar (SAR), Landsat, and Moderate Resolution Imaging Spectroradiometer (MODIS) images (Cassianides

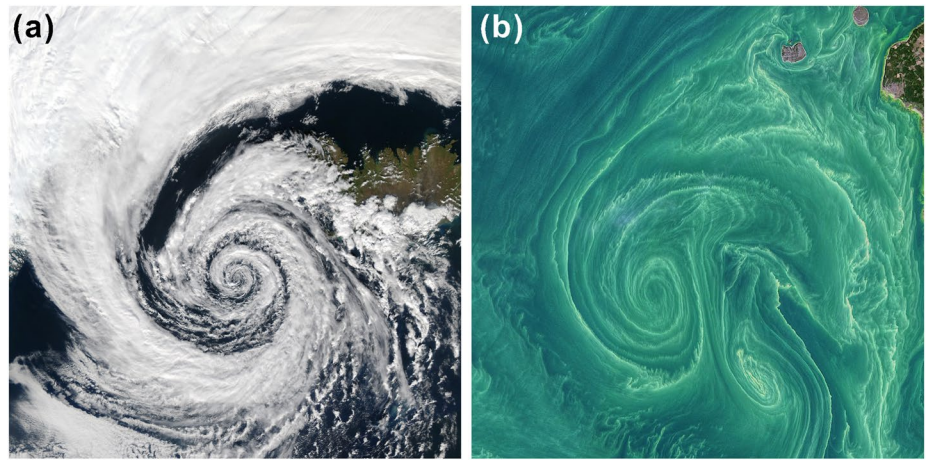

Figure 1. Spiral bands of vortex phenomena in different scales. (a) A Moderate Resolution Imaging Spectroradiometer (MODIS) image (from https://en.wikipedia.org/wiki/Cyclone) of an extratropical cyclone near Iceland observed on 4 September, 2003. Spiral white clouds are rain bands. (b) Baltic cyanobacteria from Landsat 8. The image (from https://oceancolor.gsfc.nasa.gov/gallery/717/) was collected on 15 August, 2020, and depicts surface slicks of the harmful algal bloom around the Swedish island of Gotland.

et al., 2021; Kozlov et al., 2020; Kubryakov et al., 2021; Manucharyan & Thompson, 2017). However, remote sensing can only detect eddies at the sea surface, and under specific weather and sea ice conditions.

Although many researchers have studied eddies in the Arctic Ocean, understanding of their vertical structures is not well developed. A high-resolution ocean observation technology, seismic oceanography, can quickly image the full-depth ocean using low-frequency acoustic reflection imaging (Holbrook et al., 2003). The vertical and horizontal resolutions of seismic oceanographic observations are of order 10 m, although dependent on water depth and the dominant frequency of the acoustic source (Ruddick et al., 2009). Reflections observed in the seawater column are mainly caused by vertical contrasts of seawater temperature and salinity. The seismic image can be approximately regarded as a smooth map of the vertical gradient of seawater temperature (Ruddick et al., 2009; Sallares et al., 2009).

Small-scale structures are often observed around eddies, with spiral bands being the most common. Spiral bands around eddies are found in vortex phenomena in different settings (Figure 1), such as the spiral rain bands of atmospheric tropical cyclones (Luther et al., 2010; Montgomery & Kallenbach, 1997) or the spiral bands of ocean mesoscale eddies (Z. G. Zhang & Qiu, 2020). In the early days, a spiral rain band was considered as an inertial gravity wave, but now it is interpreted as a vortex Rossby wave (VRW; Chen & Yau, 2001). Submesoscale spiral bands of ocean mesoscale eddies and spiral rain bands of tropical cyclones have a series of common kinematic and structural features and maybe the footprint of vertical movement of seawater (Z. G. Zhang & Qiu, 2020).

Similar to spiral rain bands, spiral arms of oceanic mesoscale eddies are also three-dimensional structures, inducing strong vertical velocity, therefore, they play an important role in the material and energy transports in the upper ocean. However, the width scale of the spiral bands of mesoscale eddies is approximately 10^0–10^1 km (Z. G. Zhang & Qiu, 2020). It is difficult to observe spiral bands with conventional ship-based sparse hydrographic profiles (e.g., CTD). In the past, the observations of vortex spiral bands were mostly limited to satellite observations at the sea surface, in which infrared Advanced Very High-Resolution Radiometer and SAR were employed (Karimova, 2012; Munk et al., 2000; Yamaguchi & Kawamura, 2009). Eddies appear as bright or dark spiral lines on radar images, corresponding to white eddies or black eddies, respectively (Ji et al., 2021). In addition, it was recently discovered that spiral bands can also be observed from the chlorophyll concentration at the sea surface obtained from satellites (Z. G. Zhang & Qiu, 2020).

Although satellites have been widely used to observe the characteristics of the sea surface of vortex spiral bands, observations of their associated vertical structures are rare. However, with the advantage of high horizontal sampling rate, seismic oceanography can observe mesoscale, submesoscale, and even smaller-scale oceanographic

21699291, 2022, 3, Downloaded from https://agupubs.onlinelibrary.wiley.com/doi/10.1029/2021JC017984 by Tongji University, Wiley Online Library on [05/09/2024]. See the Terms and Conditions (https://onlinelibrary.wiley.com/terms-and-conditions) on Wiley Online Library for rules of use; OA articles are governed by the applicable Creative Commons License

21699291, 2022, 3, Downloaded from https://agupubs.onlinelibrary.wiley.com/doi/10.1029/2021JC017984 by Tongji University, Wiley Online Library on [05/09/2024]. See the Terms and Conditions (https://onlinelibrary.wiley.com/terms-and-conditions) on Wiley Online Library for rules of use; OA articles are governed by the applicable Creative Commons License

phenomena (Song et al., 2021). Previous studies have used seismic oceanographic data to image eddies in different areas, such as the Gulf of Cadiz (Biescas et al., 2008; Buffett et al., 2010; Pinheiro et al., 2010), the Tyrrhenian Sea (Buffett et al., 2017), the Gulf of Stream (Gula et al., 2019), the Gulf of Alaska (Tang et al., 2014), the South China Sea (Huang et al., 2013), and the Gulf of Papagayo of Central America (Yang et al., 2021). Although these studies can resolve the vertical structure of eddies, they have rarely identified spiral arm structures. Ménesguen et al. (2012) and Song et al. (2011) observed spiral arm structures of Mediterranean eddies, but these features were not well imaged.

Using two roughly perpendicular multichannel reflection seismic sections with a time difference of 7 days in the Northwind Basin in the northeast of the Chukchi Sea, Arctic Ocean, in late September 2011, we observed a mesoscale anticyclonic eddy with submesoscale spiral bands. We also obtained concurrent velocity data with an acoustic Doppler current profiler (ADCP). The second section of this paper describes the circulations and water masses in the Chukchi Sea and its surrounding waters. The seismic data, hydrographic data, and satellite data used here are described in Section 3. Section 4 shows the results, including the mesoscale anticyclonic eddy, submesoscale spiral bands, current velocity, and the advection of this mesoscale eddy. Section 5 discusses the possible origin of the eddy, possible formation mechanism of spiral bands and the evolution of spiral bands. We summarize our findings in Section 6.

2. Oceanographic Setting

The Chukchi Sea is a broad (width 800 km) and shallow continental shelf, reaching from the Bering Strait in the south to the edge of the Arctic basin in the north (Figure 2a). The Bering Strait transports Pacific warm water northwards to the Arctic Ocean through the Chukchi Sea, driven by the North-South pressure difference (Aagaard et al., 2006). In summer and early autumn, there are two different types of Pacific warm water masses in the Chukchi Sea. The first is Alaskan Coastal Water (ACW), which is the main water mass of the Alaskan Coastal Current (ACC). The second is the combination of Anadyr Water and Bering Shelf Water, which mix in the north of Bering Strait (Corlett & Pickart, 2017) to form Bering Summer Water (BSW).

The circulation and hydrography of the Chukchi Sea is best sampled in summer when the region is generally free of sea ice. During this season, most of the currents on the Chukchi Shelf enter the interior of the Arctic Ocean through three channels: Barrow Canyon in the east, Central Channel in the middle, and Herald Canyon in the west. BSW enters the western Herald Canyon and Central Channel. The latter partially flows eastward over Hanna Shoal and joins ACW. ACW enters the Beaufort Sea through Barrow Canyon. The flow that transports Pacific water from Bering Strait to Barrow Canyon is called the Bering-Barrow Current System which is the main flow transporting Pacific water to the Arctic Ocean (Gong & Pickart, 2015). After entering the Beaufort Sea, most of the ACW turns west and joins the Chukchi Slope Current (CSC; Stabeno et al., 2018). The CSC flows westward and can reach the Herald Canyon (Stabeno et al., 2018). The CSC sometimes gets entrained into the Beaufort Gyre (Boury et al., 2020). The CSC is limited to a depth of about upper 300 m. It flows all year round, with the maximum strength in spring and summer (Stabeno et al., 2018).

According to the *T-S* diagram derived from historical CTD profiles (Figure 3), the water masses in this region can be divided into Melt Water (MW), BSW, Winter Water (WW), Remnant Winter Water (RWW), and Atlantic Water (AW). The MW has the lowest salinity. The BSW has medium salinity and high temperature. Below the BSW is the colder RWW, while the coldest water is the newly ventilated WW. Below the RWW and WW is the densest and saltiest AW. The AW and RWW/WW are bounded at a depth of ~200 m, that is, separated by the halocline.

Sea surface temperature (SST) gradually decreases from the shelf, slope to the basin, and finally reaches the freezing point (Figure 2c). To some extent, this also reflects the state of warm Pacific water entering the Arctic Ocean. The Moderate Resolution Imaging Spectroradiometer (MODIS) image in Figure 2d shows that the sea has high cloud coverage, which is not conducive to satellite observation of the sea surface.

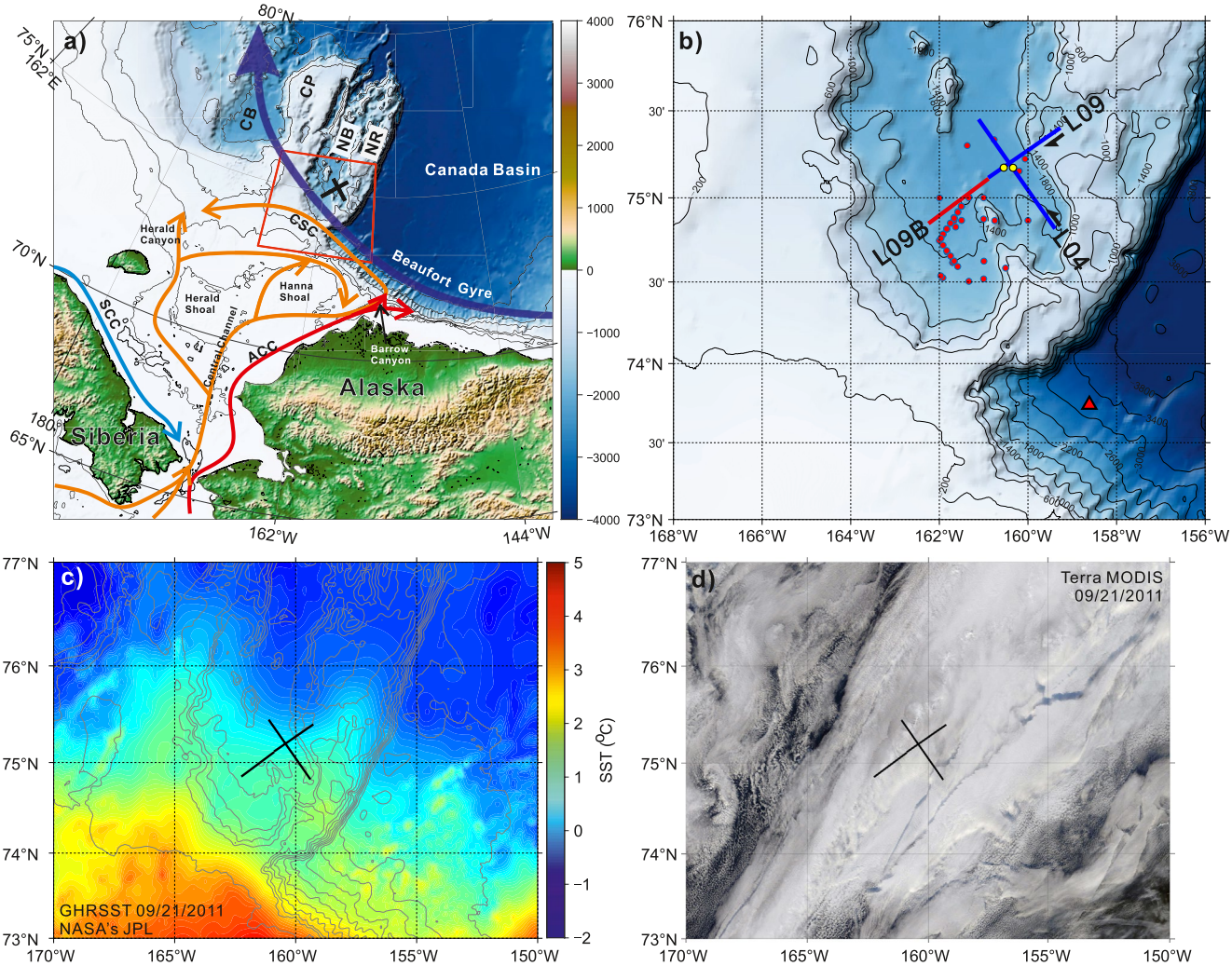

Figure 2. (a) Surface circulation and bathymetric map of the Chukchi Sea. ACC, Alaskan Coastal Current; CSC, Chukchi Slope Current; SCC, Siberian Coastal Current; NR, Northwind Ridge; NB, Northwind Basin; CP, Chukchi Plateau; CB, Chukchi Basin. The circulation is adapted from Stabeno et al. (2018). Black solid lines are seismic lines collected by R/V Marcus G Langseth in 2011. The red box is enlarged in (b). (b) Locations of seismic lines. Blue solid lines are seismic lines L04 and L09, and red solid line is line L09B. Black arrows indicate the sailing directions of the ship. 47 red circles are the historical CTD casts (described in Section 3.3). Two yellow circles are the centers of the eddy in two seismic lines. The red triangle is the location of the center of a large eddy described by Kawaguchi et al. (2012). (c) Sea Surface Temperature on 21 September, 2011 (coincident with the acquisition of seismic line L04) produced from multiple satellite data sets compiled by the Group for High-Resolution Sea Surface Temperature (GHRSST) at NASA's Jet Propulsion Laboratory (JPL). Black solid lines are seismic lines. (d) True-color image from Terra Moderate Resolution Imaging Spectroradiometer (MODIS) on 21 September, 2011 (coincident with the acquisition of seismic line L04).

3. Data

3.1. Seismic Acquisition and Processing

Multichannel seismic reflection data were provided by Marine Geoscience Data System (MGDS). The seismic reflection data were acquired during expedition MGL1112 in the northeast of Chukchi Sea from September to early October 2011 aboard the R/V Marcus G Langseth (Coakley, 2014). Three of these lines are used here: L04, L09, and L09B (see Table 1). Line L04 was acquired on 21 September, along a track from southeast to northwest. Line L09 and L09B were acquired on 29 September. They are almost collinear, along a track from northeast to southwest (Figure 2b). The acquisition times of the two lines L09 and L09B were interrupted for 6 min 8 s, leaving a gap of 1.12 km. For convenience, L09 and L09B are considered as one line L09/09B. The ship towed an airgun array with a total volume of 1,830 cubic inches. The airguns in the array were fired every 37.5 m. There were 468 hydrophones with a spacing of 12.5 m (i.e., the common mid-point [CMP] spacing is 6.25 m, that is,

21699291, 2022, 3, Downloaded from https://agupubs.onlinelibrary.wiley.com/doi/10.1029/2021JC017984 by Tongji University, Wiley Online Library on [05/09/2024]. See the Terms and Conditions (https://onlinelibrary.wiley.com/terms-and-conditions) on Wiley Online Library for rules of use; OA articles are governed by the applicable Creative Commons License

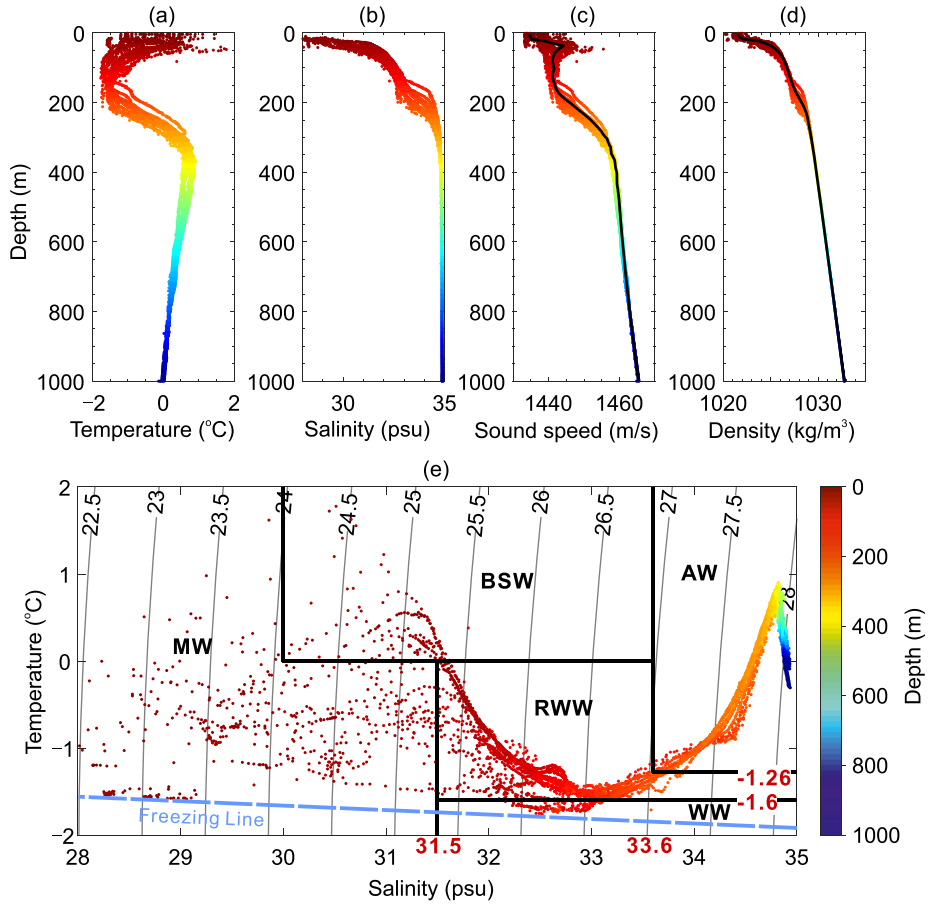

Figure 3. Hydrographic data derived from historical CTD casts (see Section 3.3). The locations of the CTD casts are shown in Figure 2b. (a) Temperature profiles. (b) Salinity profiles. (c) Sound speed profiles and (d) density calculated from temperature and salinity. Black solid lines in (c and d) are smoothed values of sound speed and density, respectively. (e) Temperature-salinity (*T*-*S*) diagram adapted from Corlett and Pickart (2017). Gray isolines are density anomalies. MW, Melt Water; BSW, Bering Summer Water; AW, Atlantic Water; RWW, Remnant Winter Water; WW, Winter Water. The color indicates the depth of the samples.

the horizontal sampling interval) in the streamer. The time sampling interval of the data was 2 ms. The minimum offsets (i.e., the shortest distance from the airgun array to the receivers) of different lines are different. The minimum offsets of L04, L09, and L09B were 226.7, 226.7, and, 206.7 m, respectively.

The seismic data processing flow of the present work is similar to that of previous studies (e.g., Ruddick et al., 2009). Since the reflected energy of the water column is much weaker than the direct wave energy, the direct wave was suppressed first to enhance the reflected energy of the stratified water column. Velocity analysis (Gunn et al., 2018) was performed by velocity scans (Figure 4). CTD-derived velocities were used as the starting points for the velocity analysis. Then normal move-out (NMO) correction was conducted based on the RMS (root mean square) velocities picked from the velocity analysis. Then the CMP gathers were extracted

Table 1
Acquisition Information and Scales of the Eddy on Seismic Sections

Line #	Eddy center			Core diameter D_c (km)	Total eddy diameter D (km)	Width of spiral bands (km)	Max depth of the core (m)
	Acquisition date and time (UTC)	Longitude	Latitude				
L04	09/21/2011 23:21:32	−160.3366	75.1742	26.129	56.875	15.373	300
L09/L09B	09/29/2011 04:42:33	−160.5466	75.1750	24.494	46.619	11.062	300

21699291, 2022, 3, Downloaded from https://agupubs.onlinelibrary.wiley.com/doi/10.1029/2021JC017984 by Tongji University, Wiley Online Library on [05/09/2024]. See the Terms and Conditions (https://onlinelibrary.wiley.com/terms-and-conditions) on Wiley Online Library for rules of use; OA articles are governed by the applicable Creative Commons License

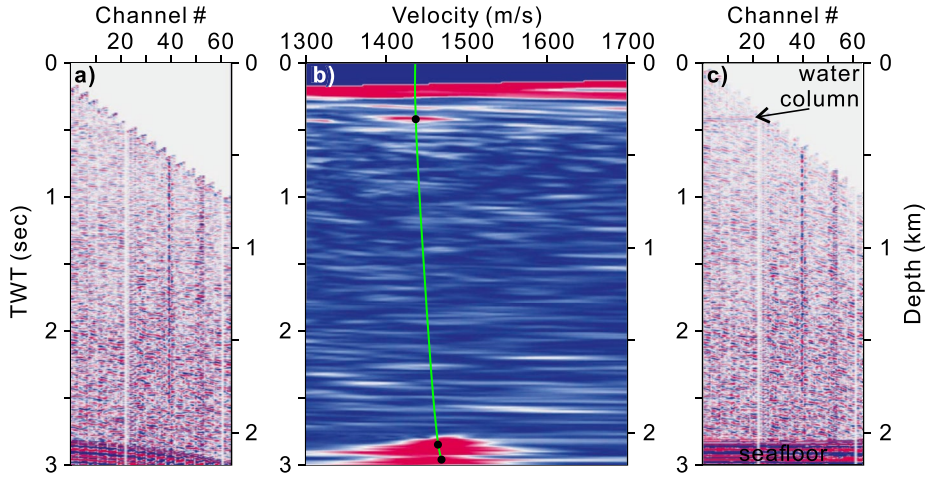

Figure 4. Velocity analysis example at 46 km in L09/09B section. (a) The common mid-point (CMP) gather before normal move-out (NMO) correction. (b) Velocity scan. The black dots are the picked velocities and the green solid line is fitted velocities. (c) The CMP gather after NMO correction.

to suppress random noise. Deconvolution of the stacked data after muting the seafloor reflections was used to increase the vertical resolution. Stolt time migration (Stolt, 1978) based on picked velocities was carried out to converge diffracted waves. Finally, two groups of F-K dip filtering (a filtering method that converts time and distance domain into the frequency and wavenumber (F-K) domain by using a two-dimensional Fourier transformation, Yilmaz, 2001) with different filtering parameters were used to attenuate the vertically coherent noise and horizontally residual direct waves, respectively. The picked velocities were used to convert the two-way travel time into depth. The processing flow chart is shown in Figure 5.

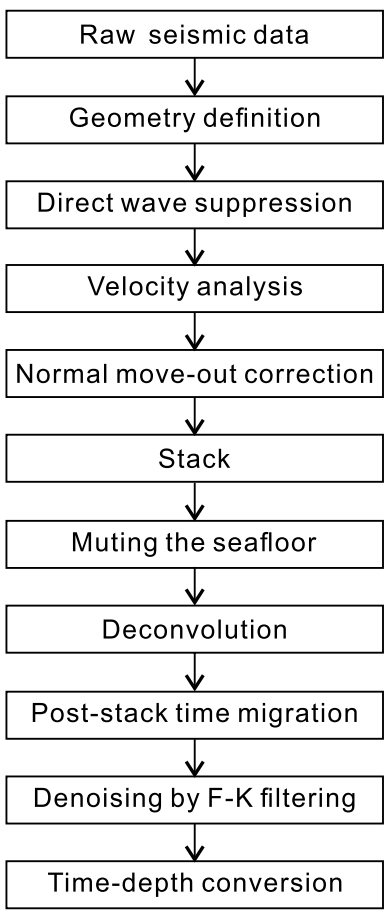

Figure 5. Processing flow chart of multi-channel reflection seismic data.

On the seismic section, the horizontal coherent reflections are the result of the vertical contrasts of seawater physical properties; however, it is also affected by the vertical resolution of acoustic waves. Since the dominant frequency of the low-frequency (10–100 Hz) airgun source is about 35 Hz and the sound velocity of seawater was assigned as 1,450 m s^{-1}, the dominant wavelength was about 40 m. Based on the Ricker criterion (Ricker, 1953), the vertical resolution of the seismic wave is ~1/4 of the dominant wavelength, that is, ~10 m. Note that, theoretically, the 1/4 wavelength is the limit of the vertical resolution, which is highly dependent on the acoustic frequency. However, true vertical resolution of the 1/4 wavelength is difficult to achieve (Hobbs et al., 2009); therefore, the water column, with different temperatures and salinities, and with vertical scales less than 10 m, cannot be resolved well in seismic sections.

3.2. Current Velocity Measured With ADCP

During seismic acquisition, an ADCP was used to measure the horizontal velocity of the seawater. ADCP data were collected with UHDAS (University of Hawaii Data Acquisition System), and processed with CODAS (Common Ocean Data Access System) software, both developed and maintained at the University of Hawaii (Firing et al., 2012). The zonal and meridional components of the measured velocity are u and v respectively, which compose the total velocity V. We can calculate the outward normal velocity $V_n = u\cos\theta - v\sin\theta$, which is perpendicular to the seismic sections, where

21699291, 2022, 3, Downloaded from https://agupubs.onlinelibrary.wiley.com/doi/10.1029/2021JC017984 by Tongji University, Wiley Online Library on [05/09/2024]. See the Terms and Conditions (https://onlinelibrary.wiley.com/terms-and-conditions) on Wiley Online Library for rules of use; OA articles are governed by the applicable Creative Commons License

θ is the azimuth of the vessel heading. The time sampling interval was ~300 s and the ship speed was ~3 m s^{-1}, hence the horizontal sampling interval is ~0.9 km. Vertically, there were 60 layers, each representing 16 m averages, with a depths ranging from 31 to 975 m.

3.3. Legacy Hydrographic Data

Because no in situ CTD data were collected simultaneously with seismic data, historical CTD data were used here. The historical CTD data is from the World Ocean Database 2018 (WOD18) and is provided by the National Environmental Information Center. The used longitude and latitude ranges are 162°W–160°W, 74.5°N–75.5°N. There were 47 qualified historical CTD casts in total, see Figure 2b for locations. The acquisition months of these CTD stations were September and early October (Northwind Basin is covered with sea ice in other months), consistent with the acquisition time of seismic data. The historical CTD data provide the background temperature and salinity. Seawater sound velocity data and density data were calculated with the Seawater toolbox of MATLAB.

3.4. Satellite Remote Sensing Data

Here, the true-color corrected reflectance image of MODIS was used to illustrate the weather conditions during seismic acquisition. MODIS data is from NASA's Worldview Snapshots website (https://wvs.earthdata.nasa.gov/).

Since the cloud coverage was quite high during data acquisition, daily average altimeter data and Sea Surface Temperature (SST) based on multi-satellite observations were used here. Gridded L4 altimeter data with a spatial resolution of 1/4° are from Copernicus Marine Environment Monitoring Center. The geostrophic velocity at the sea surface can be calculated by using the Sea Level Anomalyof the altimeter. SST data is from the Group for High-Resolution Sea Surface Temperature (GHRSST), downloaded from NASA's Jet Propulsion Laboratory (https://data.neodaas.ac.uk/visualisation/). SST data sets are multi-satellite merged products, so they are available regardless of cloud coverage. The merged SST data is a combination of low-resolution (~50 km) microwave data (during cloud cover or rainfall) and high-resolution radiometer data (during cloudless period), with a spatial resolution of about 1 km.

4. Results

The reflection characteristics of water column on the two sections can be divided into two categories (Figure 6). The reflections with depth less than 300 m are strong. Below 300 m, the reflections are very weak. The water masses involved in the reflections with strong amplitude above 300 m mainly include BSW and RWW/WW. The weak reflections below 300 m depth are mainly related to AW. The physical properties of deep water masses are relatively uniform, so the reflections are weak and discontinuous.

4.1. Mesoscale Anticyclonic Eddy

Both sections show convex lens-shaped structures with weak internal reflections (Figure 6). These are very similar to the Mediterranean eddies (Biescas et al., 2008; Song et al., 2011), so we interpret them as eddies. The two sections were almost perpendicular, and acquired about seven days apart. The characteristics of eddies are also very similar, indicating that the same eddy is displayed on the two sections (see Section 4.4 for detailed analysis). The eddy can be divided into core and boundaries. The eddy core shows very weak reflections because the physical properties (including temperature, salinity, and density) inside the core are relatively uniform. However, the eddy boundaries show a set of strong reflections, because they are located in the transition zone between core water and background water masses. This reflection structure, weak in the core and strong at the boundaries, has been observed in previous works (Biescas et al., 2008; Ménesguen et al., 2012; Song et al., 2011). The diameter of the eddy core is 24–26 km. The eddy diameter (including the boundaries) is about 47–57 km (Table 1). The

21699291, 2022, 3, Downloaded from https://agupubs.onlinelibrary.wiley.com/doi/10.1029/2021JC017984 by Tongji University, Wiley Online Library on [05/09/2024]. See the Terms and Conditions (https://onlinelibrary.wiley.com/terms-and-conditions) on Wiley Online Library for rules of use; OA articles are governed by the applicable Creative Commons License

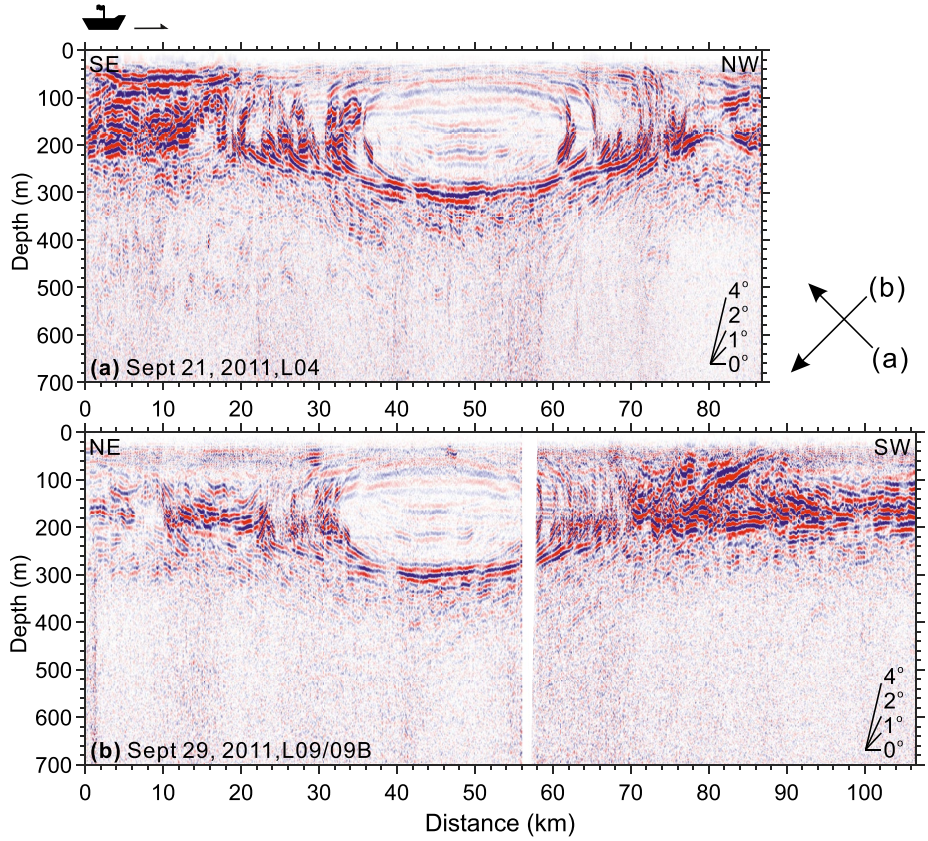

Figure 6. Seismic images of (a) Line L04 and (b) Line L09/09B. The rightward arrow above (a) indicates the vessel direction, and the arrows in the right indicate the locations and track directions of the two lines. The gap in the middle of (b) is due to the interruption of the seismic acquisition. The reference angles of the reflections are displayed in the lower right corner.

eddy core extends from near-surface (about 50 m) to a depth of about 300 m, with a core depth of about 160 m and a core thickness of about 250 m.

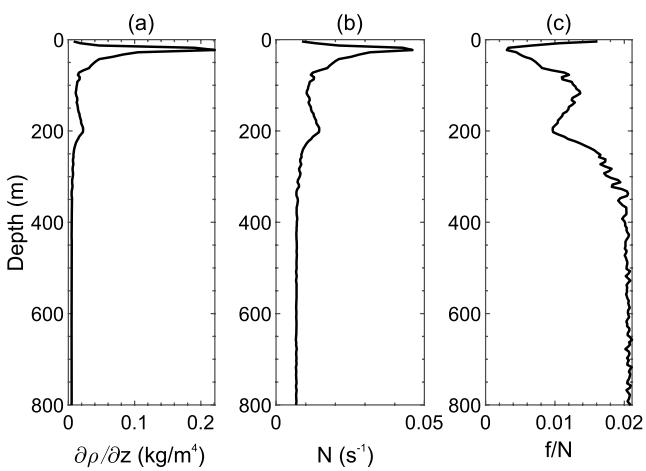

Figure 7. (a) Density gradient derived from historical CTD data. (b) The buoyancy frequency is calculated from the density gradient. (c) The ratio of Coriolis frequency to buoyancy frequency, *f/N*. The secondary strong stratification at ~200 m corresponds to the bottom of the halocline.

The horizontal scale of mesoscale eddies is larger than the first baroclinic Rossby deformation radius $L_R = NH/f$, where H is the characteristic height, and f and N are Coriolis frequency and buoyancy frequency, respectively. The higher the latitude, the smaller the characteristic height, and the weaker the density stratification, the smaller L_R will be (Chelton et al., 1998). Therefore, L_R in polar regions is typically small. Taking $N = 0.01$ s^{-1} (background buoyancy frequency, see Figure 7b), H = 250 m (the core thickness), f (75°N) = 1.4087×10^{-4} s^{-1} gives L_R = 17 km, which is consistent with the results calculated by Nurser and Bacon (2014) and Zhao et al. (2014). The eddy diameter is much larger than the local first baroclinic Rossby deformation radius, hence the eddy is mesoscale. The maximum depth of the local halocline can reach ~250 m. The mesoscale eddies are generally shallow, so most eddies are restricted above the halocline (e.g., Manley & Hunkins, 1985; Zhao et al., 2014). The maximum depth of the mesoscale eddy in this paper extends beyond the halocline due to its large scale, which is relatively rare.

Based on the geostrophic balance hypothesis, the tilt of isopycnals is caused by the horizontal shear of mesoscale currents. Therefore, the dip angle of seismic reflections can be used to estimate the geostrophic velocity of mesoscale ocean phenomena (e.g., Huang et al., 2013; Sheen et al., 2011).

21699291, 2022, 3, Downloaded from https://agupubs.onlinelibrary.wiley.com/doi/10.1029/2021JC017984 by Tongji University, Wiley Online Library on [05/09/2024]. See the Terms and Conditions (https://onlinelibrary.wiley.com/terms-and-conditions) on Wiley Online Library for rules of use; OA articles are governed by the applicable Creative Commons License

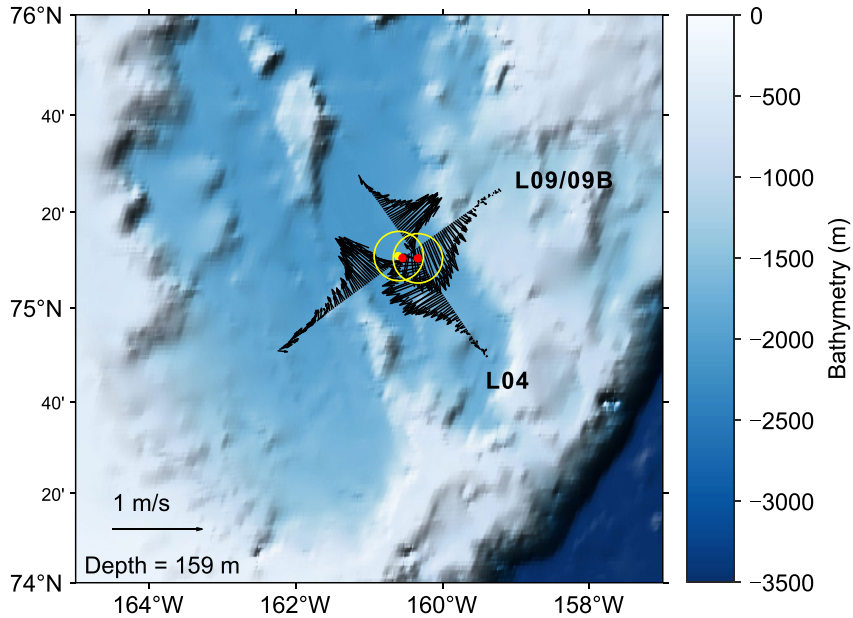

Figure 8. Horizontal current velocities (black arrows) at a depth of 159 m (about the core depth) were measured with an ADCP. The arrow in the lower left corner is the reference velocity of 1 m s^{-1}. Two red dots are the eddy centers (detailed locations are in Table 1) in the ADCP tracks. The real center (yellow dot) when line L09/09B acquisition, inferred from the velocity directions, is located in the west of the eddy center in the track. The two yellow circles are the inferred eddy core boundaries.

Although this eddy is mesoscale, the length of the reflections of the spiral bands at the eddy boundaries is short, which belongs to a submesoscale phenomenon, so it is unreasonable to estimate the geostrophic velocity of the whole eddy. Fortunately, there are ADCP-derived horizontal velocities collected simultaneously with the seismic data. As we show later, the mesoscale eddy is anticyclonic. Most of the shallow eddies in the upper 200 m of the Arctic Ocean are anticyclonic eddies. For example, Zhao et al. (2014) found that 95% of the Arctic halocline eddies are anticyclonic by using 10 yr ITP (ice tethered profilers) measurements.

The Burger number $B = (NH/fL)^2$, where L is the characteristic length of the fluid, can be used to express the ratio between density stratification in the vertical and the earth's rotation in the horizontal. Taking values of $H = 250$ m, $L = D_c = 2R_c = 26$ km (D_c and R_c are the diameter and radius of eddy core respectively), $N = 0.01$ s^{-1}, $f = 1.4087 \times 10^{-4}$ s^{-1}, we obtain $B = 0.47$, which is comparable with roughly constant values of $B \approx 1$ found for submesoscale vortices in the Arctic Ocean (D'Asaro, 1988b). Padman et al. (1990) estimated that the Burger number of a baroclinic eddy that they survey in the Southern Canadian Basin was 0.24. Our result shows that although the eddy we are describing here was not submesoscale, it had a similar aspect ratio to a submesoscale vortex. In addition, it means that rotation plays a more important role than stratification in the eddy motion (Cushman-Roisin & Beckers, 2006).

4.2. Current Velocity Measured With ADCP

The horizontal current velocity measured with an ADCP was collected simultaneously with the seismic data. As shown in Figure 8, this is a clockwise eddy (i.e., an anticyclone). The velocity directions are almost perpendicular to the vessel heading (Figure 8), which indicates that the seismic lines almost pass through the eddy center. Therefore, there is little difference between the measured velocity V and the normal velocity V_n perpendicular to the sections. In this case, V_n can be approximately considered the azimuth velocity of the eddy V_θ.

The positions of the eddy on the velocity sections are very consistent with those on the seismic sections (Figures 9b and 10b). The maximum velocities almost correspond to the radii of the eddy core (Figures 8–10). The peak velocities at the core edge, near 0.6 cm s^{-1}, are quite high. The velocities in the eddy center are near zero.

21699291, 2022, 3, Downloaded from https://agupubs.onlinelibrary.wiley.com/doi/10.1029/2021JC017984 by Tongji University, Wiley Online Library on [05/09/2024]. See the Terms and Conditions (https://onlinelibrary.wiley.com/terms-and-conditions) on Wiley Online Library for rules of use; OA articles are governed by the applicable Creative Commons License

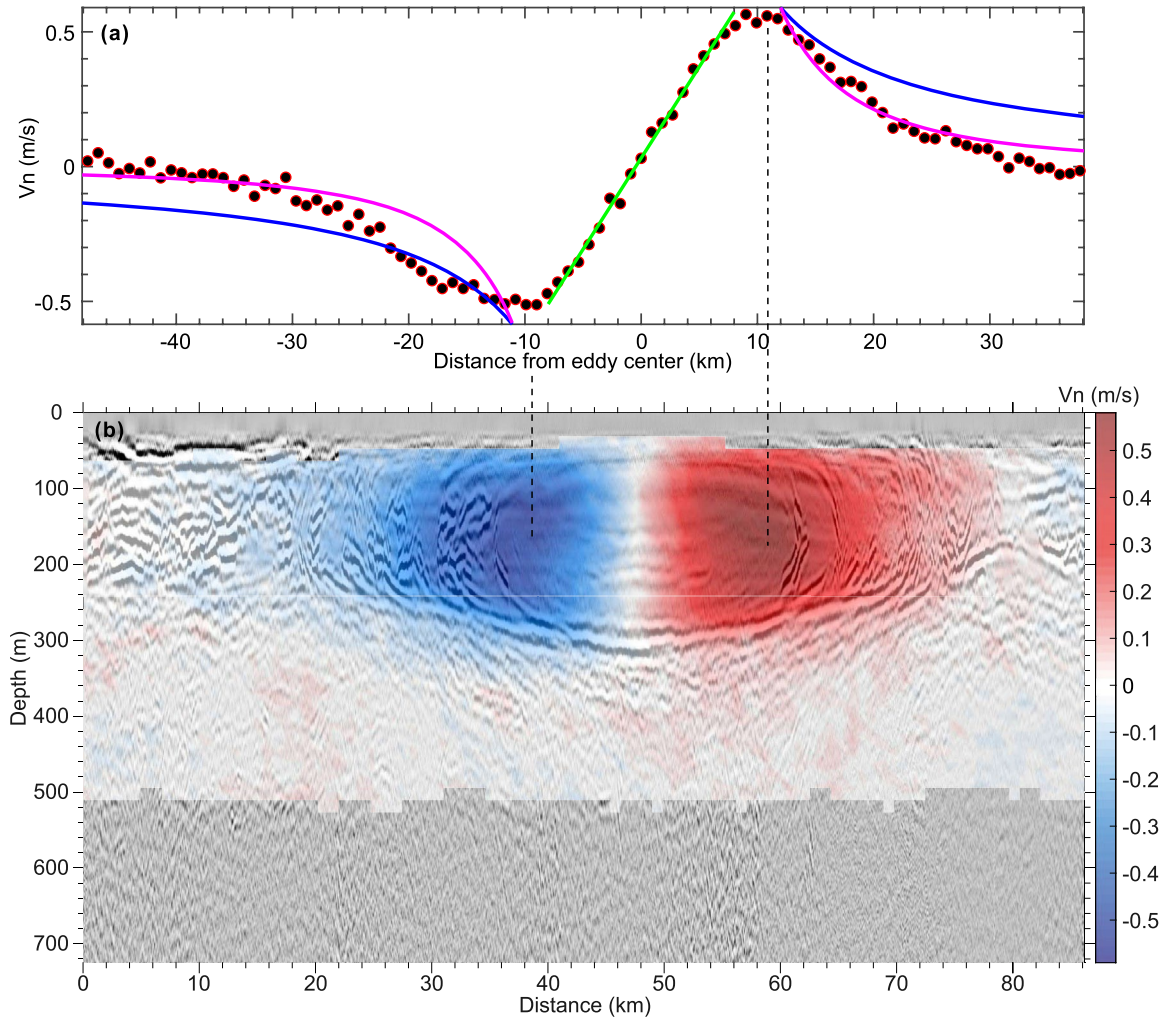

Figure 9. (a) Normal current velocities V_n (black dots) at the depth of the eddy core (159 m, Figure 8) of Line L04. Ideal curves for the Rankine vortex model are plotted, in which velocity increases proportionally to the distance r (green line) in the core ($r < R_c$), while decreases following curves of r^{-2} (magenta) rather than r^{-1} (blue) at boundaries ($r > R_c$). (b) The current velocity section (color) is overlaid on the seismic section (gray). The black dotted lines correspond to the positions of the maximum velocity. The core radius determined with the maximum velocity is smaller than that determined with the seismic reflections.

Velocity increases proportionally to the radius in the core, which is consistent with the Rankine vortex model. The Rankine vortex combines an inner core that moves as a rigid body with a vortex-free exterior (Loiseleux et al., 1998). Mathematically, the Rankine vortex is specified as:

$$V_\theta = \begin{cases} V_m \dfrac{r}{R_c}, (r \le R_c) \\ V_m \dfrac{R_c}{r}, (r > R_c) \end{cases} \quad (1)$$

where V_θ is the azimuthal velocity, V_m is the maximum azimuthal velocity, and R_c is the core radius. This model is simple. It is somewhat astonishing how well it matches real observations of vortex phenomena, such as tropical cyclones (e.g., Beer & Giannini, 1980) and oceanic eddies (e.g., Zhao et al., 2014). As shown in Figures 9a and 10a, however, the azimuthal velocities of this eddy appear to follow a curve of r^{-2} (magenta) rather than r^{-1} (blue) at the outer region. This relationship can be expressed as:

$$V_\theta = \begin{cases} V_m \dfrac{r}{R_c}, (r \le R_c) \\ V_m \dfrac{R_c^2}{r^2}, (r > R_c) \end{cases} \quad (2)$$

21699291, 2022, 3, Downloaded from https://agupubs.onlinelibrary.wiley.com/doi/10.1029/2021JC017984 by Tongji University, Wiley Online Library on [05/09/2024]. See the Terms and Conditions (https://onlinelibrary.wiley.com/terms-and-conditions) on Wiley Online Library for rules of use; OA articles are governed by the applicable Creative Commons License

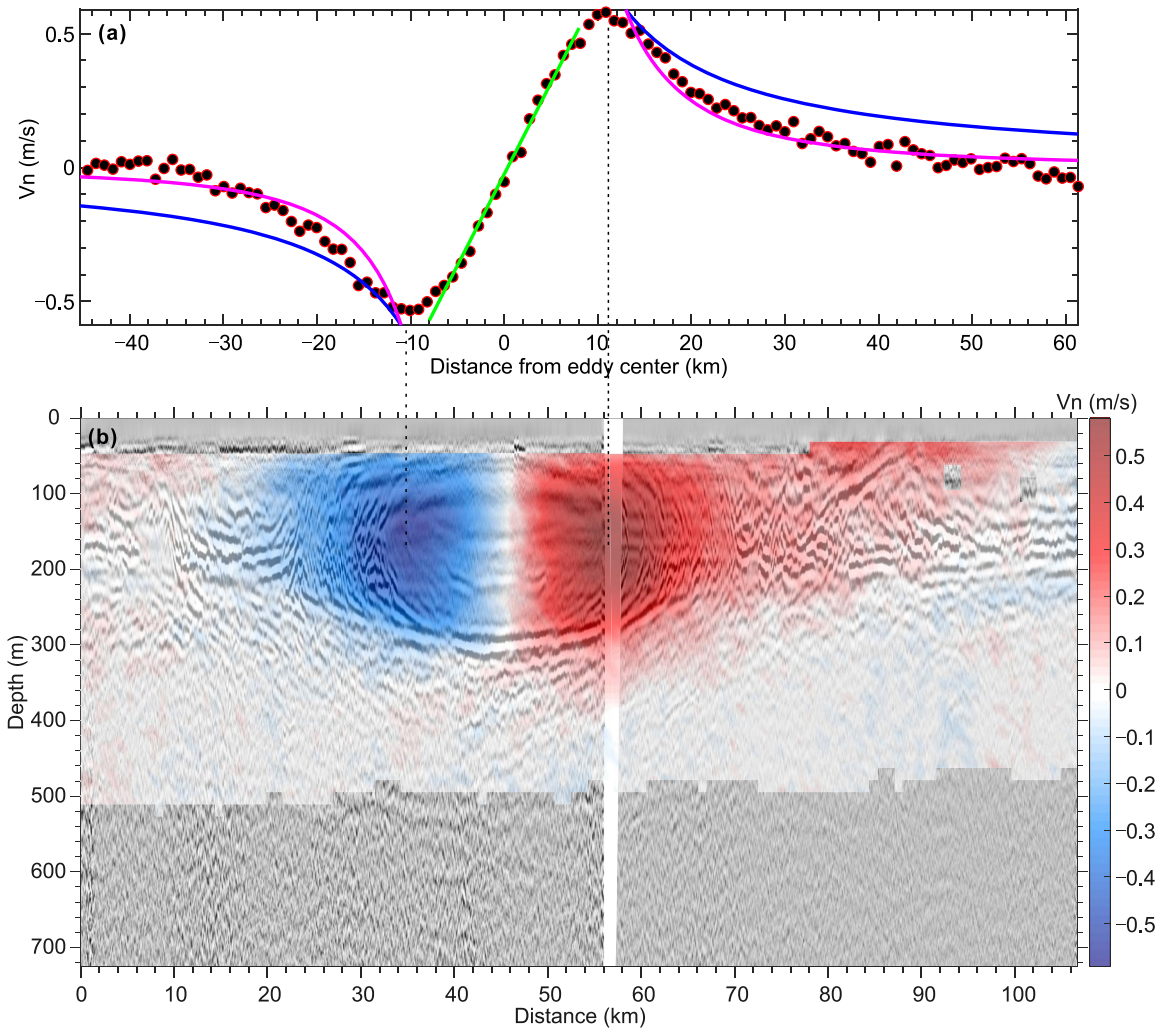

Figure 10. Same as Figure 9, except the Line L09/09B. The blank in the middle in (b) is due to the interruption of the seismic acquisition.

which indicates that the velocity outside the core decreases faster than that described by the Rankine vortex model. Similar results were obtained by Kawaguchi et al. (2012) when they studied a large eddy east of North-wind Ridge.

The eddy core is not a rigid body as a whole, but there is a transition zone at the edge of the core (Figures 9 and 10). In other words, the boundary between the core and the outside is not as sharp as described in the theory. In addition, there is a special phenomenon that the core radius determined with the maximum velocity is slightly smaller than that determined with seismic images. On the whole, the radius (~8 km) of the rigid body is less than that determined with the maximum velocity (~11 km), and the radius determined with the maximum velocity is less than that (~13 km) determined with seismic images. Seismic images are the expression of the difference of physical properties (e.g., temperature and salinity) of water masses (Ruddick et al., 2009), so the radius determined by the seismic image is better constrained. It also shows that the properties such as temperature and salinity do not completely correspond to the current velocity.

The slope of the fitting curve of the velocities in the rigid core represents the rotational angular velocity $\omega = V_m/R_c \approx 6.8 \times 10^{-5}\,s^{-1} = 0.48\,f$ (Figure 11). Therefore, the rotation period of the core is $T = 2\pi/\omega \approx 26$ hr.

21699291, 2022, 3, Downloaded from https://agupubs.onlinelibrary.wiley.com/doi/10.1029/2021JC017984 by Tongji University, Wiley Online Library on [05/09/2024]. See the Terms and Conditions (https://onlinelibrary.wiley.com/terms-and-conditions) on Wiley Online Library for rules of use; OA articles are governed by the applicable Creative Commons License

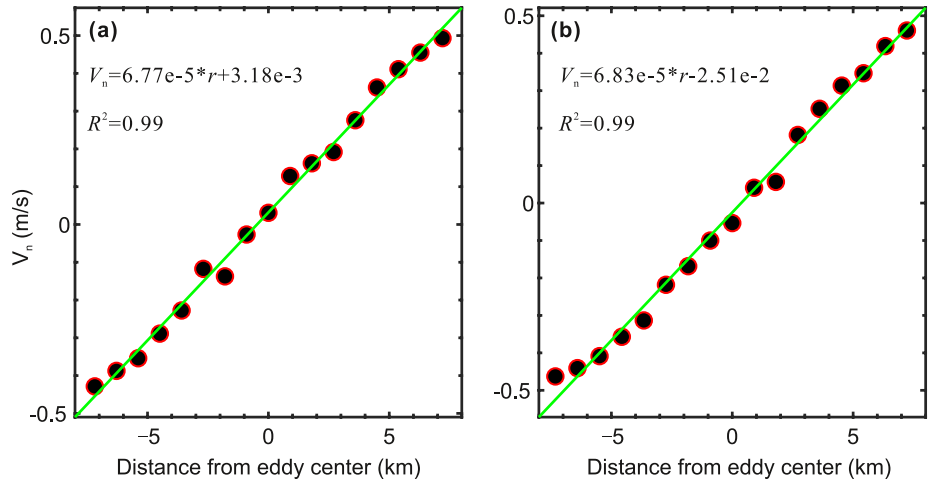

Figure 11. The measured current velocities (black dots) in the eddy core (159 m, Figure 8) in sections (a) L04 and (b) L09/09B can be fitted linearly (green solid lines). The result shows that the core is a rigid body.

4.3. Submesoscale Spiral Bands

In addition to the eddy core with weak reflections, the most obvious features on the two seismic sections are a series of strong arcuate (curved) reflections at the lateral boundaries of the eddy. The strong arcuate reflections and weak reflections appear alternately (Figure 6). Ménesguen et al. (2012) and Song et al. (2011) observed alternating strong and weak arcuate reflections around the Mediterranean eddies but they have rarely been observed in other prior studies. They believed that the spiral arms are caused by the topography or ambient currents. Motivated by structures shown in Figure 1, we interpret the alternating bands of strong and weak reflections, which are more clearly shown in Figure 12, as multiple spiral arms surrounding the eddy core. Weak reflections are uniform water masses thrown from the eddy core or relatively uniform water masses from the background, and strong reflections are the boundaries between these water masses.

Z. G. Zhang and Qiu (2020) found submesoscale spiral bands around a large number of mesoscale eddies, observed by satellites, composed of chlorophyll curls on the global sea surface. The vertical spiral bands observed from seismic sections here may be related to these sea surface spiral bands.

4.4. Advection of the Eddy

Northwind Basin is located in the southwest part of the Beaufort Gyre, which flows roughly westward over the bathymetry. Subsequent to these observations, this mesoscale eddy may have been carried westward by the CSC or the Beaufort Gyre.

The acquisition times of eddy centers of L04 and L09/09B are 7.22 days apart (Table 1). The two lines cross almost perpendicularly to each other (Figures 2b and 8). The characteristics of eddies on the two sections are also very similar, so it appears that the eddies on the two sections have the same features. The smaller scale of the latter may be since line L09/09B does not pass through the center of the eddy (e.g., Yang et al., 2021), which can be verified from the velocity directions (Figure 8). We infer that the real eddy center, during line L09/09B acquisition, is in the west of the eddy center (i.e., apparent center) seen from the ADCP track (Figure 8). Based on the apparent centers (Table 1), we can estimated the apparent moving speed of the eddy. The eddy centers of the two sections are 5.97 km apart, we calculate that the average moving speed of the eddy in 7.22 days was 0.96 cm s^{-1}. The advection azimuth was 271°, propagating to the west. Mesoscale eddies generally move horizontally with the background flow. The real advection speed would be greater than 0.96 cm/s if taking the real center into account. The typical advection velocity is about 2 cm s^{-1} (Richardson et al., 2000). Therefore, the estimated advection velocity of 0.96 cm s^{-1} or even greater is reliable.

21699291, 2022, 3, Downloaded from https://agupubs.onlinelibrary.wiley.com/doi/10.1029/2021JC017984 by Tongji University, Wiley Online Library on [05/09/2024]. See the Terms and Conditions (https://onlinelibrary.wiley.com/terms-and-conditions) on Wiley Online Library for rules of use; OA articles are governed by the applicable Creative Commons License

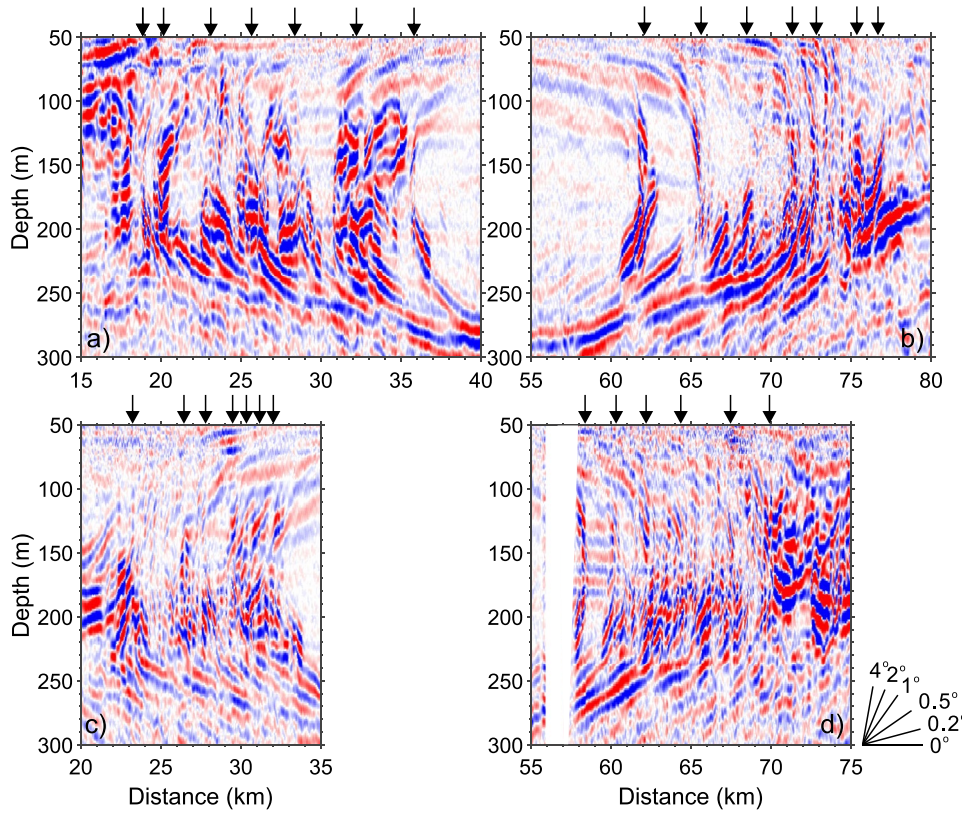

Figure 12. Zooms of seismic images for four regions of the transects shown in Figure 6. The downward arrows point to the horizontal positions of the eddy's inferred spiral arms.

It can be seen from Figures 6 and 8 that this is an axisymmetric eddy. Assuming that the eddy core is an axisymmetric rotating ellipsoid, then the volume of the eddy core $V = \frac{4}{3}\pi\frac{H}{2}R_c^2 = 89\ \text{km}^3$. This shows that this mesoscale eddy can transport ~89 km^3 core water westward at an advection velocity of about 1 cm s^{-1}. The net transport of eddy core water is, therefore, about 0.05 Sv (1 Sv = $10^6\ \text{m}^3\ \text{s}^{-1}$).

5. Discussion

5.1. A Comparison With a Previously Reported Large Eddy

On the east side of the Norhtwind Ridge, Kawaguchi et al. (2012) found a large anticyclonic eddy, named *MO*-eddy and with a diameter of more than 60 km, which extended from the surface to a depth of about 300 m. It had a core with unusual temperatures that reached 6°C, significantly warm than the surrounding 0°C water. The center location of the *MO*-eddy is shown in Figures 2b and 13. This eddy was embedded in the strong westward slope current. We find that the two eddies, observed by them and us respectively, shared some similar characteristics. The apparent diameters (60–70 and 50–60 km respectively) and apparent depths (both near-surface to ~300 m) are similar, and their shapes are both convex lenses. Kawaguchi et al. (2012) observed the eddy in early September 2010. The eddy in our study was observed in late September 2011. The observation time difference is about 380 days, and the difference of eddy center position is about 167 km. If they are the same eddy, the average westward advection speed of the eddy in about one year is about 0.5 cm s^{-1}, which is less than half of the typical translating speed of eddies (Richardson et al., 2000). The trajectory of an oceanic eddy is not a straight line, but very tortuous (Richardson et al., 2000; Stabeno et al., 2018). If the time difference is one year, the eddy likely followed a complex trajectory. Therefore, the net moving speed of the eddy is reasonable. This mesoscale eddy, with a relatively large scale, may have a long lifetime that can even reach several years (like Meddies, Richardson et al., 2000). The eddy might move from the Chukchi slope to the northwest, cross the Northwind Ridge, and then enter the Northwind Basin. The eddy trajectory may be similar with the drifter trajectory in Figure 2d of Stabeno et al. (2018). For these reasons, we speculate that the two eddies might be the same eddy. Note that, the *MO*-eddy

21699291, 2022, 3, Downloaded from https://agupubs.onlinelibrary.wiley.com/doi/10.1029/2021JC017984 by Tongji University, Wiley Online Library on [05/09/2024]. See the Terms and Conditions (https://onlinelibrary.wiley.com/terms-and-conditions) on Wiley Online Library for rules of use; OA articles are governed by the applicable Creative Commons License

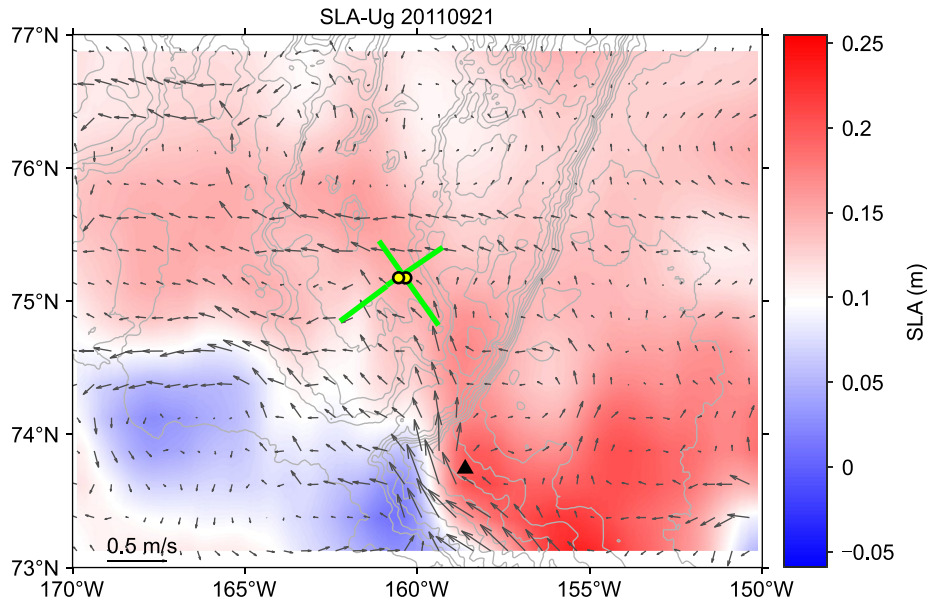

Figure 13. Sea Level Anomaly (SLA, the color map) and the surface geostrophic velocity (gray arrows) on 21 September 2011. Green solid lines are seismic lines. Two yellow circles indicate the centers of the eddy in two seismic lines. The black triangle is the location of the center of a large eddy in September 2010, observed by Kawaguchi et al. (2012). The gray contours are isobaths.

had a core with high temperature. Unfortunately, however, we do not have concurrent *T-S* data with seismics and ADCP. The eddy may have entered the Northwind Basin through slope current or Beaufort Gyre (Figure 13). The slope current meanders westward along the slope from Barrow Canyon and may reach the Herald Canyon, but does not reach the interior of the Northwind Basin (Corlett & Pickart, 2017; Stabeno et al., 2018). Sometimes the CSC may be entrained into the Beaufort Gyre (Boury et al., 2020), and the path may migrate northward. Therefore, it is difficult to determine whether the CSC or the Beaufort Gyre delivered the eddy to the Northwind Basin.

As described by Kawaguchi et al. (2012), this mesoscale eddy may have been generated from the baroclinic instability of the westward slope current. The core water with abnormally high temperature is likely from warm Pacific water which passes through the Bering Strait, passes through the Barrow Canyon (mainly the warm ACW), enters the Canadian Basin, and flows westward into the CSC. Finally, this warm eddy may be generated from the baroclinic instability of the westward slope current. The eddy observed by Kawaguchi et al. (2012) was located at the Chukchi slope and was a baroclinic eddy. Non-axisymmetric eddies tend to relax to axisymmetric states, during which the asymmetric components will irreversibly evolve to a smaller scale (Graves et al., 2006), that is, forming submesoscale filaments. We speculate that during the propagation of the baroclinic vortex on the continental slope to the deep and flat Northwind Basin, it gradually became axisymmetric. Asymmetric components separated from the core, forming vortex filaments, and finally forming spiral bands.

5.2. Possible Formation Mechanism of Spiral Bands

The results of Ménesguen et al. (2012) and Song et al. (2011) showed that although the spiral arms appear as arcs sloping, the reflections within the arms are nearly horizontal. Therefore, they believed that thermohaline intrusion dominates the spiral arms. Thermohaline intrusions are a near-horizontal interleaving structures formed between water masses with different temperature and salinity properties. As shown in Figure 12, there are near-horizontal reflections within the outer spiral arms. These near-horizontal reflections have been previously ascribed to the thermohaline intrusions (Biescas et al., 2008; Pinheiro et al., 2010). In addition, there are many independent steep reflections (up to 4° or greater) at the outer boundaries of the eddy (Figure 12). The slopes of these reflections are too large to be explained with the thermohaline intrusion theory. A plausible explanation is that there is convective shear on the isopycnals (Pinheiro et al., 2010; Song et al., 2011). For eddies, eddy stirring may cause steep reflections at the eddy boundaries (Song et al., 2011). Geostrophic eddy stirring can generate both horizontal and vertical gradients, that is, *T-S* variance is cascaded both to small horizontal and vertical

21699291, 2022, 3, Downloaded from https://agupubs.onlinelibrary.wiley.com/doi/10.1029/2021JC017984 by Tongji University, Wiley Online Library on [05/09/2024]. See the Terms and Conditions (https://onlinelibrary.wiley.com/terms-and-conditions) on Wiley Online Library for rules of use; OA articles are governed by the applicable Creative Commons License

21699291, 2022, 3, Downloaded from https://agupubs.onlinelibrary.wiley.com/doi/10.1029/2021JC017984 by Tongji University, Wiley Online Library on [05/09/2024]. See the Terms and Conditions (https://onlinelibrary.wiley.com/terms-and-conditions) on Wiley Online Library for rules of use; OA articles are governed by the applicable Creative Commons License

scales (Smith & Ferrari, 2009). The horizontal cascade is driven by the horizontal strain, which compresses the tracer isolines. The vertical cascade is caused by the tilt of tracer filaments caused by geostrophic eddy shear. The coupling between these two cascades will result in tracer filaments with a slope proportional to the ratio of the strain and shear. On a small scale, the shear-strain ratio is proportional to N/f (Smith & Ferrari, 2009), so the slope is proportional to f/N. The barotropic vortex simulation based on the fully nonlinear quasi-geostrophic frame with a constant stratification by Hua et al. (2013) showed that the maximum slope of filaments around the eddy is close to f/N. Therefore, it can be considered that the tilt of a filament with a slope exceeding f/N is caused by eddy stirring. The f/N in the upper 300 m of the Northwind Basin is ∼0.01 (Figure 7c). The corresponding dip angle is ∼0.5°. Therefore, it can be considered that the reflections with dip angles greater than 0.5° at the eddy boundaries are caused by the eddy stirring. The spiral arms in this paper are mainly reflections with great dip angles (Figures 6 and 12), especially the inner spiral arms. The widths of the spiral arms are about 1–3 km, so the spiral arms are typical submesoscale phenomena.

Z. G. Zhang and Qiu (2020) analyzed satellite observations of chlorophyll on the global sea surface and found that the submesoscale spiral bands of oceanic mesoscale eddies. Spiral rain bands of tropical cyclones have a series of similar kinematic and structural features, and spiral bands may be footprints of seawater vertical motions induced by VRWs. VRWs propagate radially outward and can reach stagnation radii where azimuthal velocities decay to ambient velocities. The stagnation radius is the maximum radius corresponding to the submesoscale spiral bands. This is very similar to spiral rain bands of tropical cyclones. In addition, the large dip angle of spiral arms indicates that spiral arms are very strong ageostrophic motions, corresponding to strong vertical velocities. Therefore, the submesoscale spiral bands play an important role in the vertical material transport in the upper ocean.

5.3. The Evolution of Spiral Bands

An eddy exchanges water with the surrounding water masses through the spiral arms, so the spiral arms are a transition zone. It seems from Figures 6 and 12 that the slopes of the reflections of the inner spiral arms are large while the slopes of the outer spiral arms are small. Therefore, we speculate that the outer spiral arm is dominated by thermohaline intrusion, and the inner spiral arm is dominated by eddy stirring. With the evolution of eddy, the outer spiral arm gradually mixes with the surrounding water masses, while the dynamic process of the inner spiral arm becomes dominated by thermohaline intrusion, so reflections gradually become nearly horizontal. The core water curls outward in the form of filaments, so the core gradually becomes smaller, and new spiral arms with steep slopes appear within the previous inner spiral arms. The core water curls outward and mixes with the surrounding water masses. Finally, the core water will be lost and the eddy dissipates. Hua et al. (2013) conducted a completely nonlinear quasi-geostrophic barotropic eddy simulation in a variable stratification background. Their results (in their Figure 8) showed that as more and more potential vorticity is stripped from the eddy core, the scale of the core decreases with time (Hua et al., 2013). Similar phenomena occur in tropical cyclones, whose concentric-eyewall structures can be considered as a part of the spiral rain bands of these cyclones. After the formation of the concentric eyewalls of a tropical cyclone, it often goes through a process of eyewall replacement in which; after the formation of the outer eyewall, it will gradually strengthen and contract inward, and finally replace the inner eyewall (Houze et al., 2007; Kuo et al., 2009; Willoughby et al., 1982). Willoughby et al. (1982) believed that these concentric spiral bands are very common, but are by no means universal phenomena, and most of them often appear in highly symmetrical strong vortex systems.

6. Conclusions

We observed the same mesoscale anticyclonic eddy by using two roughly perpendicular multi-channel reflection seismic sections seven days apart acquired in the Northwind Basin in the northeast of the Chukchi Sea in late September 2011. The eddy had a horizontal scale of ∼56 km, and it extended from the near-surface to 300 m. The volume of eddy core water was ∼89 km^3. The westward advection velocity of the eddy was about 1 cm s^{-1}. We estimate that the net transport of the core water was about 0.05 Sv. The horizontal current velocity was measured with an ADCP during acquisition of the seismic data. The positions of the eddy on the velocity sections were very consistent with those on the seismic sections. Velocity sections show that the eddy had a rigid core with a rotation period of ∼26 hr. The velocity outside the core decreased in a quadratic inverse ratio with the radius, which is different from the Rankine vortex model. The reflections at eddy boundaries are strong, while the core reflections are very weak, indicating a lack of hydrographic variability in the core. The horizontal boundaries

21699291, 2022, 3, Downloaded from https://agupubs.onlinelibrary.wiley.com/doi/10.1029/2021JC017984 by Tongji University, Wiley Online Library on [05/09/2024]. See the Terms and Conditions (https://onlinelibrary.wiley.com/terms-and-conditions) on Wiley Online Library for rules of use; OA articles are governed by the applicable Creative Commons License

of the eddy show multi-arm structures, forming spiral bands. The spiral bands that are qualitatively very similar to the spiral rain bands seen in tropical cyclones. These arms with steep slope (can up to 4°) may be caused by eddy stirring. This eddy might be the same as a large-scale baroclinic eddy observed on the Chukchi slope by Kawaguchi et al. (2012) one year earlier. The eddy core water is likely to have its source from the Pacific warm water, and has been transported to the Northwind Basin by the CSC or Beaufort Gyre.

This is the first seismic imaging of seawater columns in the Arctic Ocean, and has great significance to enhance our understanding of the vertical structure of oceanic eddies and the horizontal and vertical transports of matter. Based on comparisons with other western Arctic eddies, we expect that this eddy carries Pacific warm water, which may have an impact on the accelerated melting of the sea ice in the Arctic Ocean.

This is a detailed joint observation of water columns using current velocity sections and seismic sections. In previous studies on seismic oceanography, only Nakamura et al. (2006) used simultaneous ADCP and seismic observations, while they used only several ADCP intensity sections (not velocity sections) and two velocity casts (not sections) measured with expendable current profilers (XCP). In our study, seismic images and current velocity images of this mesoscale eddy have strong consistency, and the former show finer structures than the latter, especially at the submesoscale spiral bands around the eddy. This further verifies the advantages of the seismic oceanography method in the observation of fine structures in the ocean. We believe that more information can be obtained in the future by using simultaneous hydrographic (e.g., current velocity, temperature, and salinity) and seismic observations.

Data Availability Statement

The raw multichannel seismic reflection data are provided by MGDS (the Marine Geoscience Data System, https://www.marine-geo.org/tools/search/Files.php?data_set_uid=18256). The processed seismic data and ADCP data are available from the corresponding author (H Song). Historical CTD data are from WOD18 (World Ocean Database 2018, https://www.ncei.noaa.gov/access/world-ocean-database-select/dbsearch.html). The gridded L4 altimeter data based on multi-satellite observations are from CMEMS (Copernicus Marine Environment Monitoring Service, https://resources.marine.copernicus.eu/product-detail/SEALEVEL_GLO_PHY_L4_REP_OBSERVATIONS_008_047/INFORMATION). GHRSST data are from NASA's Jet Propulsion Laboratory (JPL, https://data.neodaas.ac.uk/visualisation/?state=a2184b). Seismic Unix is used for seismic processing. ADCP data were collected with UHDAS, and processed with CODAS software (https://currents.soest.hawaii.edu/docs/adcp_doc/index.html). Figures are created with MATLAB and M_Map softwares (https://www.eoas.ubc.ca/~rich/map.html).

Acknowledgments
ADCP data are processed by Andrew Frambach and Jules Hummon. The authors are very grateful for their help in ADCP data processing. The authors thank the captain, crew, and scientists of R/V Marcus G. Langseth expedition MGL1112 for their contributions to seismic data acquisition. Data acquisition was funded by the US National Science Foundation (Grant number: ARC09-09568). This work is funded by the National Natural Science Foundation of China (Grant number: 42176061, 41976048). The authors thank Dr. Laurie Padman and Dr. Grant George Buffett for their valuable comments and suggestions.

References

Aagaard, K., Weingartner, T. J., Danielson, S. L., Woodgate, R. A., Johnson, G. C., & Whitledge, T. E. (2006). Some controls on flow and salinity in Bering Strait. *Geophysical Research Letters*, *33*(19), L19602. https://doi.org/10.1029/2006GL026612

Beer, T., & Giannini, L. (1980). Tropical cyclone cloudbands. *Journal of the Atmospheric Sciences*, *37*(7), 1511–1520. https://doi.org/10.1175/1520-0469(1980)037<1511:Tcc>2.0.Co;2

Biescas, B., Sallares, V., Pelegri, J. L., Machin, F., Carbonell, R., Buffett, G., et al. (2008). Imaging meddy fine structure using multichannel seismic reflection data. *Geophysical Research Letters*, *35*(11), L11609. https://doi.org/10.1029/2008gl033971

Boury, S., Pickart, R. S., Odier, P., Lin, P. G., Li, M., Fine, E. C., et al. (2020). Whither the Chukchi Slope Current? *Journal of Physical Oceanography*, *50*(6), 1717–1732. https://doi.org/10.1175/Jpo-D-19-0273.1

Boyer, T. P., Baranova, O. K., Coleman, C., Garcia, H. E., Grodsky, A., Locarnini, R. A., et al. (2018). World Ocean Database 2018. NOAA Atlas NESDIS 87. https://www.ncei.noaa.gov/sites/default/files/2020-04/wod_intro_0.pdf

Buffett, G. G., Hurich, C. A., Vsemirnova, E. A., Hobbs, R. W., Sallares, V., Carbonell, R., et al. (2010). Stochastic heterogeneity mapping around a Mediterranean salt lens. *Ocean Science*, *6*(1), 423–429. https://doi.org/10.5194/os-6-423-2010

Buffett, G. G., Krahmann, G., Klaeschen, D., Schroeder, K., Sallares, V., Papenberg, C., et al. (2017). Seismic oceanography in the Tyrrhenian Sea: Thermohaline staircases, eddies, and internal waves. *Journal of Geophysical Research: Oceans*, *122*(11), 8503–8523. https://doi.org/10.1002/2017jc012726

Cassianides, A., Lique, C., & Korosov, A. (2021). Ocean eddy signature on SAR-derived sea ice drift and vorticity. *Geophysical Research Letters*, *48*(6), e2020GL092066. https://doi.org/10.1029/2020gl092066

Chelton, D. B., DeSzoeke, R. A., Schlax, M. G., El Naggar, K., & Siwertz, N. (1998). Geographical variability of the first baroclinic Rossby radius of deformation. *Journal of Physical Oceanography*, *28*(3), 433–460. https://doi.org/10.1175/1520-0485(1998)028<0433:Gvotfb>2.0.Co;2

Chen, Y. S., & Yau, M. K. (2001). Spiral bands in a simulated hurricane. Part I: Vortex Rossby wave verification. *Journal of the Atmospheric Sciences*, *58*(15), 2128–2145. https://doi.org/10.1175/1520-0469(2001)058<2128:Sbiash>2.0.Co;2

Coakley, B. (2014). Multi-Channel Seismic Shot Data from the Chukchi Sea, Arctic Ocean, acquired during the R/V Marcus G. Langseth expedition MGL1112 (2011). Interdisciplinary Earth Data Alliance (IEDA). https://doi.org/10.1594/IEDA/318256

Corlett, W. B., & Pickart, R. S. (2017). The Chukchi Slope Current. *Progress in Oceanography*, *153*, 50–65. https://doi.org/10.1016/j.pocean.2017.04.005

Cushman-Roisin, B., & Beckers, J.-M. (2006). Stratification. In *Introduction to geophysical fluid dynamics: Physical and numerical aspects* (pp. 317–334). Cambridge: Academic Press.

D'Asaro, E. A. (1988a). Generation of submesoscale vortices: A new mechanism. *Journal of Geophysical Research: Oceans*, *93*(C6), 6685–6693. https://doi.org/10.1029/JC093iC06p06685

D'Asaro, E. A. (1988b). Observations of small eddies in the Beaufort Sea. *Journal of Geophysical Research: Oceans*, *93*(C6), 6669–6684. https://doi.org/10.1029/JC093iC06p06669

Firing, E., Hummon, J. M., & Chereskin, T. K. (2012). Improving the quality and accessibility of current profile measurements in the southern ocean. *Oceanography*, *25*(3), 164–165. https://doi.org/10.5670/oceanog.2012.91

Gong, D. L., & Pickart, R. S. (2015). Summertime circulation in the eastern Chukchi Sea. *Deep-Sea Research Part II: Topical Studies in Oceanography*, *118*, 18–31. https://doi.org/10.1016/j.dsr2.2015.02.006

Graves, L. P., McWilliams, J. C., & Montgomery, M. T. (2006). Vortex evolution due to straining: A mechanism for dominance of strong, interior anticyclones. *Geophysical & Astrophysical Fluid Dynamics*, *100*(3), 151–183. https://doi.org/10.1080/03091920600792041

Gula, J., Blacic, T. M., & Todd, R. E. (2019). Submesoscale coherent vortices in the Gulf Stream. *Geophysical Research Letters*, *46*(5), 2704–2714. https://doi.org/10.1029/2019gl081919

Gunn, K. L., White, N. J., Larter, R. D., & Caulfield, C. P. (2018). Calibrated seismic imaging of eddy-dominated warm-water transport across the Bellingshausen Sea, Southern Ocean. *Journal of Geophysical Research: Oceans*, *123*, 3072–3099. https://doi.org/10.1029/2018JC013833

Hobbs, R. W., Klaeschen, D., Sallares, V., Vsemirnova, E., & Papenberg, C. (2009). Effect of seismic source bandwidth on reflection sections to image water structure. *Geophysical Research Letters*, *36*(24), L00D08. https://doi.org/10.1029/2009gl040215

Holbrook, W. S., Paramo, P., Pearse, S., & Schmitt, R. W. (2003). Thermohaline fine structure in an oceanographic front from seismic reflection profiling. *Science*, *301*(5634), 821–824. https://doi.org/10.1126/science.1085116

Houze, R. A., Chen, S. S., Smull, B. F., Lee, W. C., & Bell, M. M. (2007). Hurricane intensity and eyewall replacement. *Science*, *315*(5816), 1235–1239. https://doi.org/10.1126/science.1135650

Hua, B. L., Ménesguen, C., Le Gentil, S., Schopp, R., Marsset, B., & Aiki, H. (2013). Layering and turbulence surrounding an anticyclonic oceanic vortex: In situ observations and quasi-geostrophic numerical simulations. *Journal of Fluid Mechanics*, *731*, 418–442. https://doi.org/10.1017/jfm.2013.369

Huang, X. H., Song, H. B., Bai, Y., Liu, B. R., & Chen, J. X. (2013). Estimation of geostrophic velocity from seismic images of mesoscale eddy in the South China Sea. *Chinese Journal of Geophysics-Chinese Edition*, *56*(1), 181–187.

Ji, Y., Xu, G., Dong, C., Yang, J., & Xia, C. (2021). Submesoscale eddies in the East China Sea detected from SAR images. *Acta Oceanologica Sinica*, *40*(3), 18–26. https://doi.org/10.1007/s13131-021-1714-5

Karimova, S. (2012). Spiral eddies in the Baltic, Black, and Caspian seas as seen by satellite radar data. *Advances in Space Research*, *50*(8), 1107–1124. https://doi.org/10.1016/j.asr.2011.10.027

Kawaguchi, Y., Itoh, M., & Nishino, S. (2012). Detailed survey of a large baroclinic eddy with extremely high-temperatures in the Western Canada Basin. *Deep-Sea Research Part I: Oceanographic Research Papers*, *66*, 90–102. https://doi.org/10.1016/j.dsr.2012.04.006

Kozlov, I. E., Plotnikov, E. V., & Manucharyan, G. E. (2020). Brief communication: Mesoscale and submesoscale dynamics in the marginal ice zone from sequential synthetic aperture radar observations. *The Cryosphere*, *14*(9), 2941–2947. https://doi.org/10.5194/tc-14-2941-2020

Kubryakov, A. A., Kozlov, I. E., & Manucharyan, G. E. (2021). Large mesoscale eddies in the Western Arctic Ocean from satellite altimetry measurements. *Journal of Geophysical Research: Oceans*, *126*, e2020JC016670. https://doi.org/10.1029/2020JC016670

Kuo, H. C., Chang, C. P., Yang, Y. T., & Jiang, H. J. (2009). Western North Pacific Typhoons with concentric eyewalls. *Monthly Weather Review*, *137*(11), 3758–3770. https://doi.org/10.1175/2009mwr2850.1

Loiseleux, T., Chomaz, J. M., & Huerre, P. (1998). The effect of swirl on jets and wakes: Linear instability of the Rankine vortex with axial flow. *Physics of Fluids*, *10*(5), 1120–1134. https://doi.org/10.1063/1.869637

Luther, D. S., Flament, P., Chavanne, C. P., & Gurgel, K.-W. (2010). Observations of vortex Rossby waves associated with a mesoscale cyclone. *Journal of Physical Oceanography*, *40*(10), 2333–2340. https://doi.org/10.1175/2010jpo4495.1

Manley, T. O., & Hunkins, K. (1985). Mesoscale eddies of the Arctic Ocean. *Journal of Geophysical Research*, *90*(C3), 4911. https://doi.org/10.1029/JC090iC03p04911

Manucharyan, G. E., & Thompson, A. F. (2017). Submesoscale sea ice-ocean interactions in marginal ice zones. *Journal of Geophysical Research: Oceans*, *122*(12), 9455–9475. https://doi.org/10.1002/2017jc012895

Ménesguen, C., Hua, B. L., Carton, X., Klingelhoefer, F., Schnürle, P., & Reichert, C. (2012). Arms winding around a meddy seen in seismic reflection data close to the Morocco coastline. *Geophysical Research Letters*, *39*(5), L05604. https://doi.org/10.1029/2011gl050798

Montgomery, M. T., & Kallenbach, R. J. (1997). A theory for vortex Rossby-waves and its application to spiral bands and intensity changes in hurricanes. *Quarterly Journal of the Royal Meteorological Society*, *123*(538), 435–465. https://doi.org/10.1002/qj.49712353810

Muench, R. D., Gunn, J. T., Whitledge, T. E., Schlosser, P., & Smethie, W. (2000). An Arctic Ocean cold-core eddy. *Journal of Geophysical Research: Oceans*, *105*(C10), 23997–24006. https://doi.org/10.1029/2000jc000212

Munk, W., Armi, L., Fischer, K., & Zachariasen, F. (2000). Spirals on the sea. *Proceedings of the Royal Society A: Mathematical, Physical & Engineering Sciences*, *456*, 1217–1280. https://doi.org/10.1098/rspa.2000.0560

Nakamura, Y., Noguchi, T., Tsuji, T., Itoh, S., Niino, H., & Matsuoka, T. (2006). Simultaneous seismic reflection and physical oceanographic observations of oceanic fine structure in the Kuroshio extension front. *Geophysical Research Letters*, *33*(23), L23605. https://doi.org/10.1029/2006gl027437

Nurser, A. J. G., & Bacon, S. (2014). The Rossby radius in the Arctic Ocean. *Ocean Science*, *10*(6), 967–975. https://doi.org/10.5194/os-10-967-2014

Padman, L., Levine, M., Dillon, T., Morison, J., & Pinkel, R. (1990). Hydrography and microstructure of an Arctic cyclonic eddy. *Journal of Geophysical Research: Oceans*, *95*(C6), 9411–9420. https://doi.org/10.1029/JC095iC06p09411

Pinheiro, L. M., Song, H. B., Ruddick, B., Dubert, J., Ambar, I., Mustafa, K., et al. (2010). Detailed 2-D imaging of the Mediterranean outflow and Meddies off W Iberia from multichannel seismic data. *Journal of Marine Systems*, *79*(1–2), 89–100. https://doi.org/10.1016/j.jmarsys.2009.07.004

Richardson, P. L., Bower, A. S., & Zenk, W. (2000). A census of Meddies tracked by floats. *Progress in Oceanography*, *45*(2), 209–250. https://doi.org/10.1016/S0079-6611(99)00053-1

Ricker, N. (1953). Wavelet contraction, wavelet expansion, and the control of seismic resolution. *Geophysics*, *18*(4), 769–792. https://doi.org/10.1190/1.1437927

21699291, 2022, 3, Downloaded from https://agupubs.onlinelibrary.wiley.com/doi/10.1029/2021JC017984 by Tongji University, Wiley Online Library on [05/09/2024]. See the Terms and Conditions (https://onlinelibrary.wiley.com/terms-and-conditions) on Wiley Online Library for rules of use; OA articles are governed by the applicable Creative Commons License

Ruddick, B., Song, H. B., Dong, C. Z., & Pinheiro, L. (2009). Water column seismic images as maps of temperature gradient. *Oceanography*, *22*(1), 192–205. https://doi.org/10.5670/oceanog.2009.19

Sallares, V., Biescas, B., Buffett, G., Carbonell, R., Danobeitia, J. J., & Pelegri, J. L. (2009). Relative contribution of temperature and salinity to ocean acoustic reflectivity. *Geophysical Research Letters*, *36*(24), L00D06. https://doi.org/10.1029/2009gl040187

Sheen, K. L., White, N., Caulfield, C. P., & Hobbs, R. W. (2011). Estimating geostrophic shear from seismic images of oceanic structure. *Journal of Atmospheric and Oceanic Technology*, *28*(9), 1149–1154. https://doi.org/10.1175/Jtech-D-10-05012.1

Smith, K. S., & Ferrari, R. (2009). The production and dissipation of compensated thermohaline variance by mesoscale stirring. *Journal of Physical Oceanography*, *39*(10), 2477–2501. https://doi.org/10.1175/2009jpo4103.1

Song, H. B., Chen, J. X., Pinheiro, L. M., Ruddick, B., Fan, W. H., Gong, Y., et al. (2021). Progress and prospects of seismic oceanography. *Deep-Sea Research Part I*, *177*, 103631. https://doi.org/10.1016/j.dsr.2021.103631

Song, H. B., Pinheiro, L. M., Ruddick, B., & Teixeira, F. C. (2011). Meddy, spiral arms, and mixing mechanisms viewed by seismic imaging in the Tagus Abyssal Plain (SW Iberia). *Journal of Marine Research*, *69*(4–6), 827–842. https://doi.org/10.1357/002224011799849309

Spall, M. A., Pickart, R. S., Fratantoni, P. S., & Plueddemann, A. J. (2008). Western Arctic shelfbreak eddies: Formation and transport. *Journal of Physical Oceanography*, *38*(8), 1644–1668. https://doi.org/10.1175/2007jpo3829.1

Stabeno, P., Kachel, N., Ladd, C., & Woodgate, R. (2018). Flow patterns in the eastern Chukchi Sea: 2010–2015. *Journal of Geophysical Research: Oceans*, *123*(2), 1177–1195. https://doi.org/10.1002/2017jc013135

Stolt, R. H. (1978). Migration by Fourier-transform. *Geophysics*, *43*(1), 23–48. https://doi.org/10.1190/1.1440826

Tang, Q. S., Gulick, S. P. S., & Sun, L. T. (2014). Seismic observations from a Yakutat eddy in the northern Gulf of Alaska. *Journal of Geophysical Research: Oceans*, *119*(6), 3535–3547. https://doi.org/10.1002/2014JC009938

Willoughby, H. E., Clos, J. A., & Shoreibah, M. G. (1982). Concentric eyewalls, secondary wind maxima, and the evolution of the hurricane vortex. *Journal of the Atmospheric Sciences*, *39*(2), 395–411. https://doi.org/10.1175/1520-0469(1982)039<0395:Cewswm>2.0.Co;2

Yamaguchi, S., & Kawamura, H. (2009). SAR-imaged spiral eddies in Mutsu Bay and their dynamic and kinematic models. *Journal of Oceanography*, *65*(4), 525–539. https://doi.org/10.1007/s10872-009-0045-5

Yang, S., Song, H. B., Fan, W. H., & Wu, D. (2021). Submesoscale features of a cyclonic eddy in the Gulf of Papagayo, Central America. *Chinese Journal of Geophysics-Chinese Edition*, *64*(4), 1328–1340. https://doi.org/10.6038/cjg2021O0204

Yilmaz, O. (2001). *Seismic data analysis: Processing, inversion, and interpretation of seismic data* (pp. 905–907). Tulsa, OK: Society of Exploration Geophysicists.

Zhang, X., Dai, H., Zhao, J., & Yin, H. (2019). Generation mechanism of an observed submesoscale eddy in the Chukchi Sea. *Deep Sea Research Part I: Oceanographic Research Papers*, *148*, 80–87. https://doi.org/10.1016/j.dsr.2019.04.015

Zhang, Z. G., & Qiu, B. (2020). Surface chlorophyll enhancement in mesoscale eddies by submesoscale spiral bands. *Geophysical Research Letters*, *47*(14), e2020GL088820. https://doi.org/10.1029/2020GL088820

Zhang, Z. G., Wang, W., & Qiu, B. (2014). Oceanic mass transport by mesoscale eddies. *Science*, *345*(6194), 322–324. https://doi.org/10.1126/science.1252418

Zhao, M. N., Timmermans, M. L., Cole, S., Krishfield, R., Proshutinsky, A., & Toole, J. (2014). Characterizing the eddy field in the Arctic Ocean halocline. *Journal of Geophysical Research: Oceans*, *119*(12), 8800–8817. https://doi.org/10.1002/2014jc010488

21699291, 2022, 3, Downloaded from https://agupubs.onlinelibrary.wiley.com/doi/10.1029/2021JC017984 by Tongji University, Wiley Online Library on [05/09/2024]. See the Terms and Conditions (https://onlinelibrary.wiley.com/terms-and-conditions) on Wiley Online Library for rules of use; OA articles are governed by the applicable Creative Commons License